

## Temperature dependence of phonons in Pd<sub>3</sub>Fe through the Curie temperature

F. C. Yang,<sup>1,\*</sup> O. Hellman,<sup>1</sup> M. S. Lucas,<sup>1</sup> H. L. Smith,<sup>1</sup> C. N. Saunders,<sup>1</sup> Yuming Xiao,<sup>2</sup> Paul Chow,<sup>2</sup> and B. Fultz<sup>1</sup>

<sup>1</sup>*Department of Applied Physics and Materials Science, California Institute of Technology, Pasadena, California 91125, USA*

<sup>2</sup>*HPCAT, Geophysical Laboratory, Carnegie Institution of Washington, Argonne, Illinois 60439, USA*



(Received 13 November 2017; revised manuscript received 23 May 2018; published 3 July 2018)

Iron phonon partial densities of states of Pd<sub>3</sub><sup>57</sup>Fe were measured from room temperature through the Curie transition at 500 K using nuclear resonant inelastic x-ray scattering. The experimental results were compared to *ab initio* spin-polarized calculations that model the finite-temperature thermodynamic properties of *L*<sub>12</sub>-ordered Pd<sub>3</sub>Fe with stochastically generated atomic displacements, coupled with magnetic special quasirandom structures of noncollinear magnetic moments. The scattering measurements and first-principles calculations show that the Fe partial vibrational entropy is close to what is predicted by the quasiharmonic approximation owing to a cancellation of effects. Anharmonicity and a magnon-phonon interaction approximately cancel a ferromagnetic optical phonon stiffening.

DOI: [10.1103/PhysRevB.98.024301](https://doi.org/10.1103/PhysRevB.98.024301)

### I. INTRODUCTION

Advances in the design of magnetic materials are enabled by understanding how their properties depend on the external conditions of temperature, pressure, and magnetic field. In particular, it is important to understand their thermodynamic properties over a range of temperatures. This requires modeling a magnetic material not only in its ground state at 0 K but also in its magnetically disordered states at finite temperatures.

Progress has been made in first-principles simulations of magnetic disorder in materials [1]. Recent approaches to modeling the paramagnetic state of magnetic materials include disordered local moment molecular dynamics (DLM-MD) [2,3], spin-space averaging [4–7], and spin dynamics [8–10]. With such advances, a computational study accounting for the interaction of the magnetic and atomic degrees of freedom, which has been demonstrated to provide a more complete calculation of the Gibbs free energy of magnetic materials [11], is now within reach. In the present study of the thermal excitations in Pd<sub>3</sub>Fe, magnetic disorder is included in the finite-temperature calculations of vibrational thermodynamic properties.

Fe-Pd alloys have been the subject of numerous studies owing to their magnetic and mechanical behavior. Properties of interest include a martensitic transformation in Fe-rich alloys [7,12,13], noncollinear magnetic structures [14–17], and Invar behavior [18]. Pd<sub>3</sub>Fe, a ferromagnetic metallic compound with an fcc-based *L*<sub>12</sub> structure and a Curie temperature of approximately 500 K [19], exhibits Invar behavior under applied pressure [20]. This compound also exhibits an anomalous dependence of phonon frequencies and volume with pressure as a consequence of a magnetic transition [16,21]. In the present work, we investigate this interaction between lattice dynamics and magnetic excitations at temperatures through the Curie temperature using nuclear resonant inelastic x-ray scattering and first-principles calculations.

### II. METHODS

#### A. Experiment

Measurements were performed on the *L*<sub>12</sub>-ordered Pd<sub>3</sub><sup>57</sup>Fe sample used in a pressure-induced Invar experiment [20], which was prepared by arc melting Pd of 99.95% purity and <sup>57</sup>Fe of 95.38% isotopic enrichment before the newly synthesized Pd<sub>3</sub><sup>57</sup>Fe sample was cold rolled to a thickness of 25 μm. This ordered sample was further annealed with a heat treatment at 873 K for 18 h under vacuum, 773 K for 54 h, and subsequent cooling to 293 K over 2 h. X-ray diffraction confirmed the *L*<sub>12</sub> structure and long-range order, and Mössbauer spectroscopy confirmed the short-range order (shown in the Supplemental Material [22]).

Nuclear resonant inelastic x-ray scattering (NRIXS) measurements were performed on Pd<sub>3</sub><sup>57</sup>Fe at seven temperatures from 298 to 786 K. NRIXS is a low-background technique that provides direct access to the phonon partial density of states (PDOS) of <sup>57</sup>Fe [23,24]. Measurements were performed at beamline 16ID-D of the Advanced Photon Source at Argonne National Laboratory. The synchrotron flashes had durations of 70 ps and were separated by 153 ns. Electronic scattering occurs within femtoseconds of the pulse arrival at the sample. The relatively long lifetime of the nuclear resonant state ( $\tau = 141$  ns) allowed for a clear separation of the prompt electronic scattering from the delayed resonant scattering.

The Pd<sub>3</sub><sup>57</sup>Fe foil sample was held in vacuum under active evacuation in a resistive heating furnace with a Kapton window for x-ray transmission. Errors in the values of the temperature ranged from  $\pm 10$  to  $\pm 27$  K. The ambiguity comes from comparing the furnace thermocouple measurements to NRIXS-derived detailed balance temperature calculations following the procedure described in the literature [25,26].

An avalanche photodiode was positioned at approximately 90° from the incident beam to collect incoherently reradiated photons. The energy was scanned from  $-80$  to  $+80$  meV around 14.413 keV, the resonant energy of <sup>57</sup>Fe, in several scans that were combined for final analysis. The energy resolution

\*Corresponding author: [cyang2@caltech.edu](mailto:cyang2@caltech.edu)

of all NRIXS measurements was measured to be 2.2 meV (FWHM) at the elastic line. The PHOENIX software package was used to extract the  $^{57}\text{Fe}$  PDOS from the measured NRIXS spectra [25].

Nuclear forward scattering (NFS) measurements were collected immediately prior to NRIXS scans. The NFS spectra provide a measure of the magnetic state of  $\text{Pd}_3^{57}\text{Fe}$  using an avalanche photodiode in the path of the forward-scattered x-ray beam to measure the transmitted intensity as a function of time.

In situ synchrotron x-ray diffraction (XRD) measurements were performed concurrently with the NRIXS and NFS measurements with the same monochromatic beam of 14.413 keV x rays and a Mar CCD detector plate. Results from synchrotron XRD were used to obtain lattice parameters for the quasiharmonic (QH) approximation of the Fe PDOS.

## B. Computation: Phonon calculation

Phonon frequencies at elevated temperatures were calculated with a variation of the temperature-dependent effective potential (TDEP) method [27–29]. In the TDEP procedure, the Born-Oppenheimer surface of a material at a given temperature is sampled with *ab initio* molecular dynamics (AIMD). The energies, displacements, and forces on thermally displaced atoms are recorded over time. With these energy-force-displacement data sets, force constants are obtained with a least-squares fit of the following model Hamiltonian to the potential-energy surface at a given temperature:

$$\mathcal{H} = U_0 + \frac{1}{2!} \sum_{ij\alpha\beta} \Phi_{ij}^{\alpha\beta} u_i^\alpha u_j^\beta + \frac{1}{3!} \sum_{ijk\alpha\beta\gamma} \Phi_{ijk}^{\alpha\beta\gamma} u_i^\alpha u_j^\beta u_k^\gamma, \quad (1)$$

where  $u_i$  is the displacement of atom  $i$  and  $\alpha\beta\gamma$  are Cartesian components. The temperature-dependent  $U_0$  is a fit parameter for the baseline of the potential-energy surface [28]. The quadratic force constants  $\Phi_{ij}$  from the thermally displaced atoms capture nonharmonic effects such as magnon-phonon interactions at a given temperature and are used to calculate phonon frequencies  $\omega_s$  shifted by these effects [28], where  $s$  is an index for phonon modes. The cubic force constants  $\Phi_{ijk}$  capture phonon-phonon interactions (PPI) that contribute to the broadening and additional shifts of phonon modes [29].

The same procedure was applied in this work, except the Born-Oppenheimer surface was sampled through multiple density functional theory (DFT) calculations on supercells of thermally displaced atoms generated by stochastic sampling of a canonical ensemble. For a cell of  $N_a$  atoms with mass  $m_i$ , a harmonic normal-mode transformation was used to generate positions  $\{u_i\}$  consistent with a canonical ensemble:

$$u_i = \sum_{s=1}^{3N_a} \epsilon_{is} \langle A_{is} \rangle \sqrt{-2 \ln \xi_1} \sin(2\pi \xi_2), \quad (2)$$

where  $\omega_s$  and  $\epsilon_{is}$  are the eigenvalues and eigenvectors of phonon modes  $s$  obtained from trial force constants calculated from short AIMD simulations. Other quantities include  $\xi_n$ , uniformly distributed random numbers between 0 and 1 producing the Box-Muller transform, and  $\langle A_{is} \rangle$ , the thermal average of

the normal-mode amplitudes [30,31]:

$$\langle A_{is} \rangle = \underbrace{\sqrt{\frac{\hbar(2n_s + 1)}{2m_i\omega_s}}}_{\text{quantum}} \approx \underbrace{\frac{1}{\omega_s} \sqrt{\frac{k_B T}{m_i}}}_{\text{classical}}, \quad (3)$$

where  $n_s = (e^{\hbar\omega_s/k_B T} - 1)^{-1}$  is the thermal occupation of mode  $s$  and  $\hbar\omega \ll k_B T$  denotes the classical limit at high temperatures. The stochastically generated thermal displacements from Eqs. (2) and (3) sample the Born-Oppenheimer surface in the stochastically initialized temperature-dependent effective potential (s-TDEP) method [27–29,32].

This method approximates the inclusion of zero-point motion not included in AIMD simulations and connects seamlessly to the classical limit at high temperature. The s-TDEP procedure can be used to calculate force constants capturing anomalous high-temperature effects [32] to low-temperature quantum effects [33,34] at a much lower computational cost than what is required of AIMD. The force constants calculated with this method are numerically converged with respect to the number of configurations and supercell size. Fewer configurations would be required if the size of the supercell were larger. The convergence of the force constants and the baseline  $U_0$  was further ensured by repeating DFT calculations on new snapshots generated by Eq. (2), where the frequencies  $\omega_s$  were calculated from the force constants from the previous iteration of s-TDEP. The weakness of the s-TDEP method is that it relies on Gaussian distributions of coordinates generated by Eq. (2).

The *ab initio* spin-polarized DFT calculations with spin-orbit coupling were performed with the projector augmented-wave [35] formalism as implemented in VASP [36,37]. All calculations used a  $3 \times 3 \times 3$  supercell with 108 atoms, a  $2 \times 2 \times 2$  Monkhorst-Pack [38]  $k$ -point grid, and a plane-wave energy cutoff of 520 eV. The exchange-correlation energy was calculated with the Perdew-Burke-Ernzerhof functional [39]. It was observed from calculations and from past experiments [40–42] that the magnetic moment of Pd atoms in  $\text{Pd}_3\text{Fe}$  is small compared to that of Fe atoms. The Pd moments were approximated as zero.

At a given temperature, the forces and energies of 25 stochastically generated supercells were calculated at five volumes within  $-2.5$  to  $+5\%$  around the 0 K equilibrium volume through three iterations of the s-TDEP procedure. For each volume, the Helmholtz free energy  $F(V, T)$  was calculated:

$$F(V, T) = U_0(V, T) + F_{\text{vib}}(V, T). \quad (4)$$

$U_0(V, T)$  is the baseline from Eq. (1).  $F_{\text{vib}}(V, T)$  is from lattice vibrations:

$$F_{\text{vib}} = \int_0^\infty g(\omega) \left\{ k_B T \ln \left[ 1 - \exp\left(-\frac{\hbar\omega}{k_B T}\right) \right] + \frac{\hbar\omega}{2} \right\} d\omega, \quad (5)$$

where  $g(\omega)$  is the phonon density of states calculated from the phonons in the first Brillouin zone,

$$g(\omega) = \sum_s \delta(\omega - \omega_s). \quad (6)$$

At a given temperature, the equilibrium volume  $V_T$  was obtained through the minimization of the Helmholtz free energy  $F(T, V)$ . The force constants were then interpolated to this volume, giving us phonon frequencies that capture volume expansion and temperature-dependent nonharmonic effects.

We then corrected our phonon frequencies  $\omega_s(T, V_T)$  by calculating the linewidths  $\Gamma_s$  and shifts  $\Delta_s$  arising from anharmonicity, or phonon-phonon interactions. This required the many-body perturbation calculation of the real and imaginary parts of the phonon self-energy [43,44]  $\Sigma(\Omega) = \Delta(\Omega) + i\Gamma(\Omega)$ , where  $E = \hbar\Omega$  is a probing energy. The imaginary component  $\Gamma(\Omega)$  is

$$\begin{aligned} \Gamma_s(\Omega) = & \frac{\hbar\pi}{16} \sum_{s's''} |\Phi_{ss's''}|^2 \{ (n_{s'} + n_{s''} + 1) \\ & \times \delta(\Omega - \omega_{s'} - \omega_{s''}) + (n_{s'} - n_{s''}) \\ & \times [\delta(\Omega - \omega_{s'} + \omega_{s''}) - \delta(\Omega + \omega_{s'} - \omega_{s''})] \}, \quad (7) \end{aligned}$$

and the real component is obtained by a Kramers-Kronig transformation,

$$\Delta(\Omega) = \frac{1}{\pi} \int \frac{\Gamma(\omega)}{\omega - \Omega} d\omega. \quad (8)$$

The imaginary component of the self-energy is a sum over all possible three-phonon interactions, where  $\Phi_{ss's''}$  is the three-phonon matrix element determined from the cubic force constants  $\Phi_{ijk}$ .  $\Gamma(\Omega)$  and  $\Delta(\Omega)$  were calculated with a  $36 \times 36 \times 36$   $q$  grid.

Anharmonic phonon DOS curves were calculated with the real and imaginary parts of the phonon self-energy:

$$g_{\text{anh}}(\omega) = \sum_s \frac{2\omega_s \Gamma_s(\omega)}{[\omega^2 - \omega_s^2 - 2\omega_s \Delta_s(\omega)]^2 + 4\omega_s^2 \Gamma_s^2(\omega)}. \quad (9)$$

It is noted that if both  $\Delta$  and  $\Gamma$  go to zero, Eq. (9) reduces to Eq. (6).

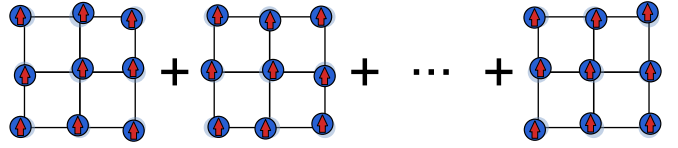
This procedure was implemented to calculate two sets of phonon dispersions and DOS: for Pd<sub>3</sub>Fe maintaining complete ferromagnetic order at 0, 300, 480, 600, and 800 K [illustrated in Fig. 1(a)] and for Pd<sub>3</sub>Fe with increasing magnetic disorder at 300, 480, and 800 K [illustrated in Fig. 1(b)]. Pd<sub>3</sub>Fe is expected to be completely ferromagnetic only at 0 K. The calculations of the completely ferromagnetic Pd<sub>3</sub>Fe at nonzero temperatures were performed for comparison with computations with magnetic disorder.

For comparison with the s-TDEP phonon spectra, the phonon energies predicted by the QH approximation were calculated by interpolation of the 0 K quadratic force constants to volumes obtained from the minimization of the free energy. This ‘‘QH DFT model’’ assumes that the only temperature dependence in Eqs. (4) and (5) is from volume expansion and the Planck distribution. The QH DFT model excludes the anharmonic corrections provided by Eqs. (7) and (8).

### C. Computation: Magnetic disorder

The magnetic disorder from thermal fluctuations was modeled with special quasirandom structures (SQSs) [45] of noncollinear Fe magnetic moments. The magnetic SQSs mimic the most relevant local correlation functions of random magnetic structures [46], where the correlation function of the

(a) 0 K, Ferromagnetic



(b) 800 K, Paramagnetic

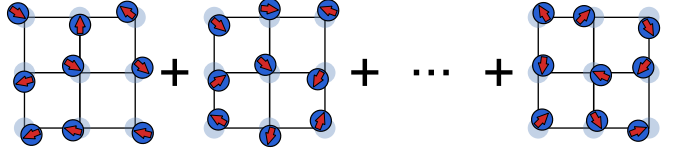


FIG. 1. (a) Schematic of supercells with Fe atoms (dark blue) stochastically displaced from their ideal positions (light blue) in the 0 K ferromagnetic calculations, where the magnetic moments (red arrows) are aligned in the same direction. (b) Supercells with randomly oriented magnetic moments and stochastically displaced Fe atoms in the 800 K paramagnetic calculations. Each set of randomly oriented magnetic moments is a magnetic special quasirandom structure (SQS). Pd atoms are not shown for this illustration.

coordination shell  $\alpha$  is

$$\Pi_\alpha = \frac{1}{N_\alpha} \sum_{i,j \in \alpha} \mathbf{e}_i \cdot \mathbf{e}_j, \quad (10)$$

where  $\mathbf{e}_i = \mathbf{m}_i / \|\mathbf{m}_i\|$  is a unit vector in the direction of the magnetic moment  $\mathbf{m}_i$  on site  $i$  and  $N_\alpha$  is the number of magnetic moment pairs in the coordination shell  $\alpha$ . This use of SQSs with noncollinear Fe magnetic moments is related to the disordered local moment (DLM) model, where magnetic disorder is modeled with randomly oriented local magnetic moments [47–52].

A histogram of magnetic SQSs was generated by simulated annealing, where Fe magnetic moments were flipped into random orientations until the local correlation functions matched target correlation functions. These bins were of increasing levels of magnetic disorder, from completely ordered to completely disordered. In the same bin of the histogram, the set of magnetic SQSs  $\{\lambda\}$  were equivalent in their correlation functions.

All correlation functions of magnetic SQSs modeling complete ferromagnetic order equaled 1 ( $\Pi_\alpha = 1 \forall \alpha$ ), and the resulting Fe magnetic moments were aligned in the same direction. All correlation functions of magnetic SQSs modeling complete magnetic disorder equaled zero ( $\Pi_\alpha = 0 \forall \alpha$ ), and the resulting Fe magnetic moments were randomly oriented. The correlation functions for magnetic SQSs from a bin that was between complete order and complete disorder had values between 0 and 1. For a given bin, the generated magnetic SQSs had an averaged normalized magnetization,

$$\langle M/M_0 \rangle_{\text{SQS}} = \frac{1}{N_m} \left\| \sum_\lambda \left( \sum_i \mathbf{m}_i \right) \right\|, \quad (11)$$

where  $N_m$  is a normalization constant.

For the phonon calculations of Pd<sub>3</sub>Fe with increasing magnetic disorder, we coupled the s-TDEP procedure with these

magnetic SQSs. For a given temperature  $T$ , 25 stochastically sampled supercells  $\{\kappa\}$  with thermal atomic displacements characteristic of  $T$  were generated. Separately, 25 magnetic SQSs  $\{\lambda\}$  were selected from a bin where the SQSs have an averaged normalized magnetization  $\langle M/M_0 \rangle_{\text{SQS}}$  approximately equal to the normalized magnetization  $M(T)/M_0$  expected at temperature  $T$ . A spin-polarized DFT calculation was performed on a supercell  $\kappa$  paired with a magnetic SQS  $\lambda$ . The forces from these spin-polarized DFT calculations on the ensemble of SQS-supercell  $(\kappa, \lambda)$  pairs, illustrated in Fig. 1(b), are used to obtain force constants used in the calculation of phonon dispersions and DOS, as described previously. This computational method can be considered to be a stochastic ensemble-averaged variant of DLM-MD [2,3] with local spin correlations.

For the calculations at 800 K, the magnetic structure was treated as a random distribution of magnetic moments characterized by the vanishing of the spin-correlation functions ( $\Pi_\alpha = 0 \forall \alpha$ ), so that the average magnetization  $\langle M \rangle_{\text{SQS}}$  is zero, in accordance with the DLM model. The force constants calculated at 800 K were interpolated to a volume that minimized a modified Helmholtz free energy  $F(T, V)$ ,

$$F(T, V) = U_0(T, V) + F_{\text{vib}}(T, V) + F_{\text{mag}}(T, V), \quad (12)$$

where  $F_{\text{mag}}(T, V)$  is the magnetic free energy. Because there is no exact formulation for the magnetic free energy, this free energy was approximated with a mean-field term,

$$F_{\text{mag}}(T, V) = -T S_{\text{mag}} = -k_B T \ln[\langle m(V) \rangle + 1], \quad (13)$$

where  $\langle m(V) \rangle$  is the average magnitude of the magnetic moments in units of  $\mu_B$ . The magnetic entropy  $S_{\text{mag}}$  is the maximum orientational disorder of magnetic moments in the paramagnetic state for systems with local magnetic moments. This approach is widely used to describe the magnetic entropy of paramagnetic systems [6,53].

For calculations at 300 and 480 K, the magnetic structures were sampled so the averaged normalized magnetizations  $\langle M/M_0 \rangle_{\text{SQS}}$  were approximately equal to normalized hyperfine fields  $H(T)/H_0$  obtained from Mössbauer spectroscopy measurements performed in this study and by Longworth [19], as seen in Fig. 2. Because there is no reliable method for calculating the magnetic free energy of Pd<sub>3</sub>Fe at intermediate temperatures, force constants were calculated at volumes obtained by scaling the volume calculated at 800 K by volumes obtained from synchrotron x-ray diffraction measurements.

### III. RESULTS

#### A. Nuclear forward scattering

The NFS spectra measured from the Pd<sub>3</sub><sup>57</sup>Fe sample are shown in Fig. 3. The NFS spectrum at 298 K exhibits the clear magnetic beat pattern expected from a magnetically ordered material, similar to a previous NFS measurement of Pd<sub>3</sub><sup>57</sup>Fe at ambient conditions [20]. The amplitudes and periods of the magnetic beats diminish with temperature, and the magnetic beats disappear above 485 K, consistent with a second-order phase transition in which the magnetic order continuously decreases through the Curie temperature. The remaining beats above 485 K are from the thickness of the sample.

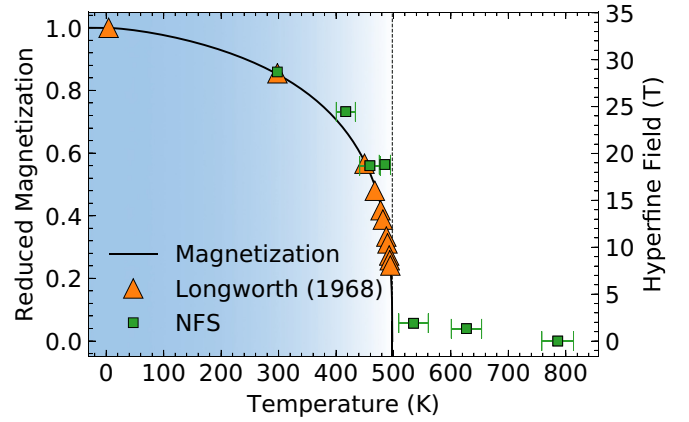


FIG. 2. The magnetization curve of Pd<sub>3</sub>Fe obtained from an empirical fit of a magnetic shape function [54] to hyperfine magnetic fields obtained from the NFS spectra in this study (green) and Mössbauer data from a study by Longworth [19] (orange). The shaded region indicates the temperature range where Pd<sub>3</sub>Fe exhibits ferromagnetic order.

A quantitative analysis of the NFS spectra was performed with the software package CONUSS [25,55]. The refined fits overlie the experimental spectra in Fig. 3. Parameters extracted from these fits include the hyperfine field  $H$ , shown

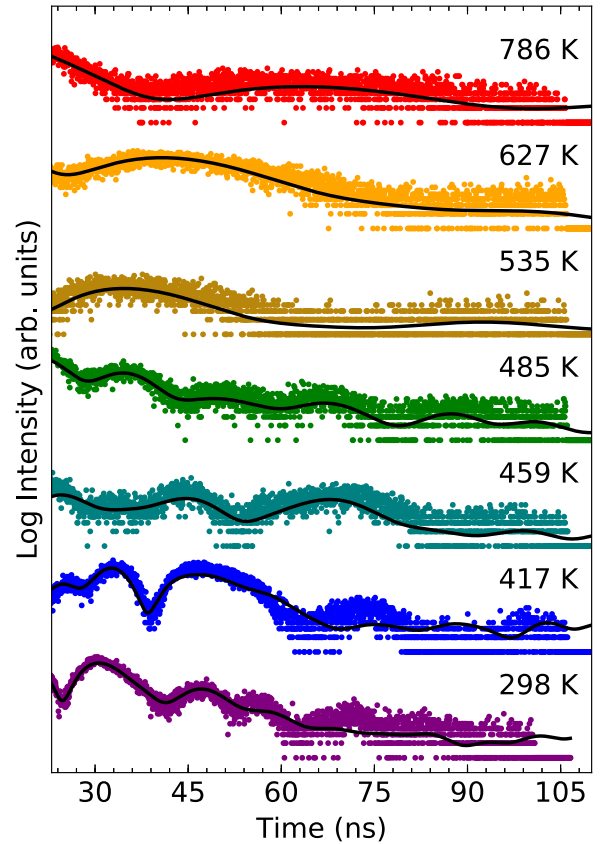


FIG. 3. The <sup>57</sup>Fe nuclear forward-scattering spectra from L1<sub>2</sub>-ordered Pd<sub>3</sub>Fe at several temperatures. The fits (black curves) overlie experimental data (points). The spectra are displayed using a log scale and offset for clarity.

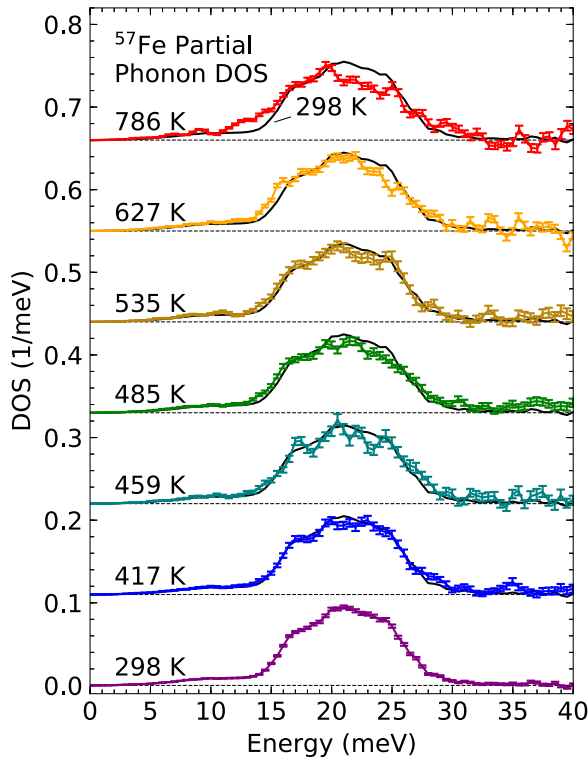


FIG. 4. The normalized  $^{57}\text{Fe}$  PDOS extracted from NRIXS measurements at various temperatures. The spectra from measurements above 298 K are offset and compared with the 298 K PDOS (black curve). Error bars are from counting statistics.

together with the magnetization of Pd<sub>3</sub>Fe in Fig. 2, and the Lamb-Mössbauer factor, shown in the Supplemental Material [22]. The decrease in the hyperfine field of Pd<sub>3</sub><sup>57</sup>Fe with temperature is in agreement with the hyperfine fields measured by Longworth [19], and the decrease in this quantity with temperature tracks the decrease in magnetization through the Curie temperature.

### B. Phonons

The  $^{57}\text{Fe}$  PDOS curves measured from the Pd<sub>3</sub><sup>57</sup>Fe sample are shown in Fig. 4. The PDOSs do not show significant energy shifts below the Curie temperature. The phonons begin to show a small but significant thermal softening beyond the Curie temperature, made apparent when the 627 and 786 K PDOSs are compared with the 298 K curve in Fig. 4. This trend is seen more clearly with the average Fe phonon energies calculated from the  $^{57}\text{Fe}$  PDOS, shown in Fig. 5. These phonon shifts are similar to the experimental trends observed in the ferromagnetic cementite through the Curie temperature [56]. It is noted that the quality of the high-temperature  $^{57}\text{Fe}$  PDOS at 786 K was impacted by reduced counting statistics.

The phonon DOS curves calculated at 0, 300, 480, and 800 K with s-TDEP are shown in Fig. 6. The phonon DOS curves soften with temperature, although features like the peak at 21 meV in the Fe PDOS or at 25 meV in the Pd PDOS do not soften until the Curie temperature. The s-TDEP phonon

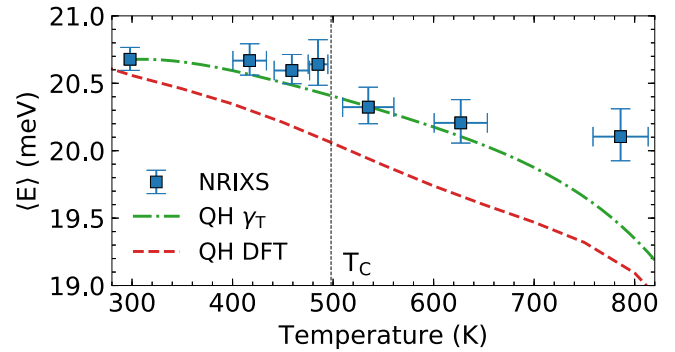


FIG. 5. Average energies of the Fe PDOS from NRIXS measurements (blue squares) plotted with the average Fe phonon energies from the Grüneisen parameter model (green line) and the QH DFT model (red line).

DOS curves also exhibit a thermal broadening that is most prominent at 800 K, indicative of PPI [43,44,57,58].

Figures 7(a) and 7(b) show thermal trends from experiment and computation, respectively. The difference spectra shown in both panels are in reasonable agreement with each other, indicating that the NRIXS measurements and s-TDEP calculations capture similar thermal trends in Pd<sub>3</sub>Fe.

### C. Nonharmonic behavior

The experimental nonharmonic behavior was analyzed by comparing the measured  $^{57}\text{Fe}$  PDOS with Fe PDOS curves predicted by QH approximations. The experimental QH phonon frequencies  $\omega_i^{\text{QH}}(T)$  were calculated with the Grüneisen parameter model (referred to as the QH  $\gamma_T$  model), a QH model using a thermal Grüneisen parameter  $\bar{\gamma}_T$ , averaged for all phonon modes:

$$\omega_i^{\text{QH}}(T) = \omega_i^{298\text{K}} \left( 1 - \bar{\gamma}_{\text{th}} \frac{V_T - V_{298\text{K}}}{V_{298\text{K}}} \right), \quad (14)$$

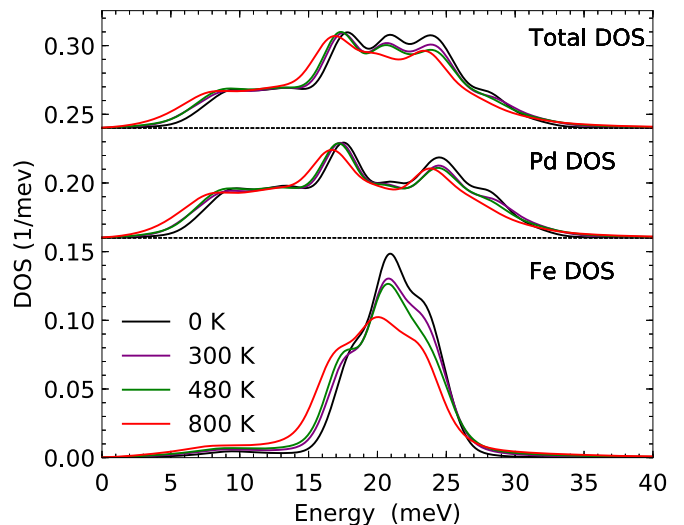


FIG. 6. Total, Pd partial, and Fe partial phonon DOS curves of Pd<sub>3</sub>Fe calculated with the s-TDEP method from 0 to 800 K.

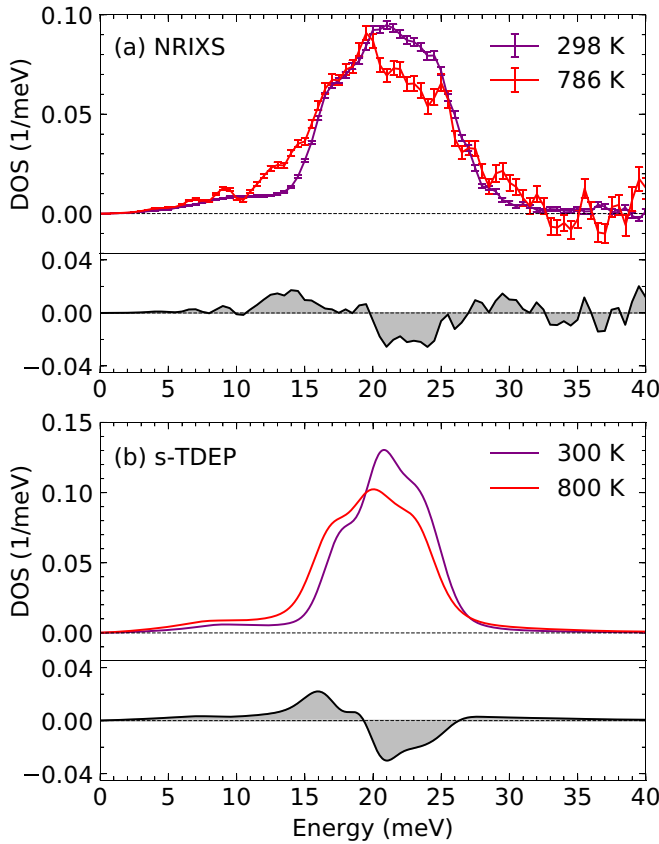


FIG. 7. (a) NRIXS  $^{57}\text{Fe}$  PDOS curves compared at 298 and 786 K. (b) s-TDEP Fe PDOS curves compared at 300 and 800 K. Phonon difference spectra are shown for both NRIXS and s-TDEP.

with the 298 K  $^{57}\text{Fe}$  phonons used for scaling the Grüneisen parameter in the QH  $\gamma_T$  model. The volumes at elevated temperatures  $V_T$  were calculated from the lattice parameters determined from our synchrotron XRD measurements, together with lattice parameters reported by Jääskeläinen and Suoninen [59]. The thermal Grüneisen parameter was calculated from bulk properties of  $\text{Pd}_3\text{Fe}$ :

$$\bar{\gamma}_{\text{th}}(T) = \frac{\alpha(T)K_T(T)\nu(T)}{C_V(T)}, \quad (15)$$

where  $K_T(T)$  is the bulk modulus,  $\alpha(T)$  is the linear thermal expansion,  $\nu(T)$  is the crystalline volume per atom, and  $C_V(T)$  is the heat capacity at constant volume. The quantities  $\alpha(T)$  and  $\nu(T)$  were calculated from volumes obtained from synchrotron XRD and from Jääskeläinen and Suoninen. The heat capacity was calculated by integrating the total phonon DOS calculated by s-TDEP. The bulk modulus was previously determined by Winterrose *et al.* through energy-dispersive x-ray diffraction [20].

The average Fe phonon energies from the QH  $\gamma_T$  and QH DFT models are plotted in Fig. 5. The Fe phonons calculated with the two QH models soften more strongly with temperature than the NRIXS  $^{57}\text{Fe}$  PDOS, indicating that there is a nonharmonic stiffening in  $\text{Pd}_3\text{Fe}$  opposing the softening from thermal expansion.

Thermodynamic consequences of nonharmonic phonons were assessed by calculating the Fe partial vibrational entropy

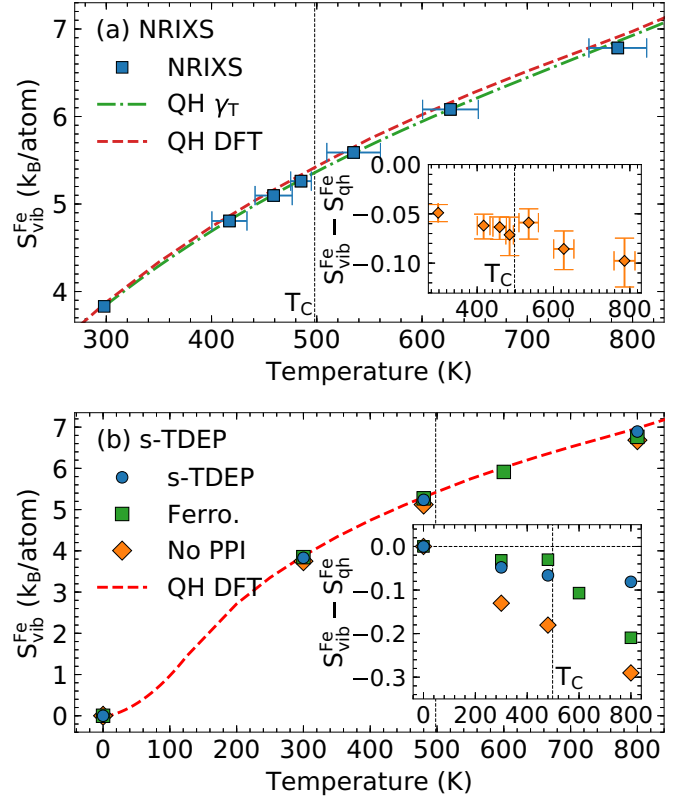


FIG. 8. (a) The Fe partial vibrational entropy from the NRIXS measurements compared with the entropy from the Grüneisen parameter model (QH  $\gamma_T$ ) and the QH DFT model. (b) The s-TDEP Fe partial vibrational entropy calculated for  $\text{Pd}_3\text{Fe}$  with changing magnetic order (blue), ferromagnetic order (green), and the absence of phonon-phonon interactions (orange). The red line is the entropy from the QH DFT model. The insets in (a) and (b) show the nonharmonic contributions to the vibrational entropy.

$S_{\text{vib}}^{\text{Fe}}$ , which contributes to the total thermodynamic entropy. This  $S_{\text{vib}}^{\text{Fe}}$  is obtained from the Fe PDOS as

$$S_{\text{vib}}^{\text{Fe}}(T) = 3k_B \int g_T^{\text{Fe}}(\epsilon) \{ (n+1) \ln(n+1) - n \ln(n) \} d\epsilon, \quad (16)$$

where  $k_B$  is the Boltzmann constant,  $g_T^{\text{Fe}}(E)$  is the Fe PDOS at temperature  $T$ , and  $n$  is a Planck distribution evaluated at  $T$  for a given energy  $E$ . This expression provides accurate entropy values that include both quasiharmonic effects and nonharmonic effects [57].

The  $S_{\text{vib}}^{\text{Fe}}(T)$  are plotted in Fig. 8(a). The quasiharmonic vibrational entropy  $S_{\text{vib}}^{\text{Fe, qh}}$ , also shown in the figure, was calculated by substituting the Fe PDOS from the QH  $\gamma_T$  and QH DFT models into Eq. (16). The agreement is surprisingly good, considering that the QH model neglects so many nonharmonic effects, including those shown in Fig. 8(b).

Figure 8(b) shows the Fe partial vibrational entropy calculated with the phonons calculated with s-TDEP, together with the Fe partial vibrational entropy without effects from PPI. This quantity, labeled “No PPI,” was calculated by substituting the Fe PDOS calculated with Eq. (6) into Eq. (16). Also shown in Fig. 8(b) is the Fe partial vibrational entropy for

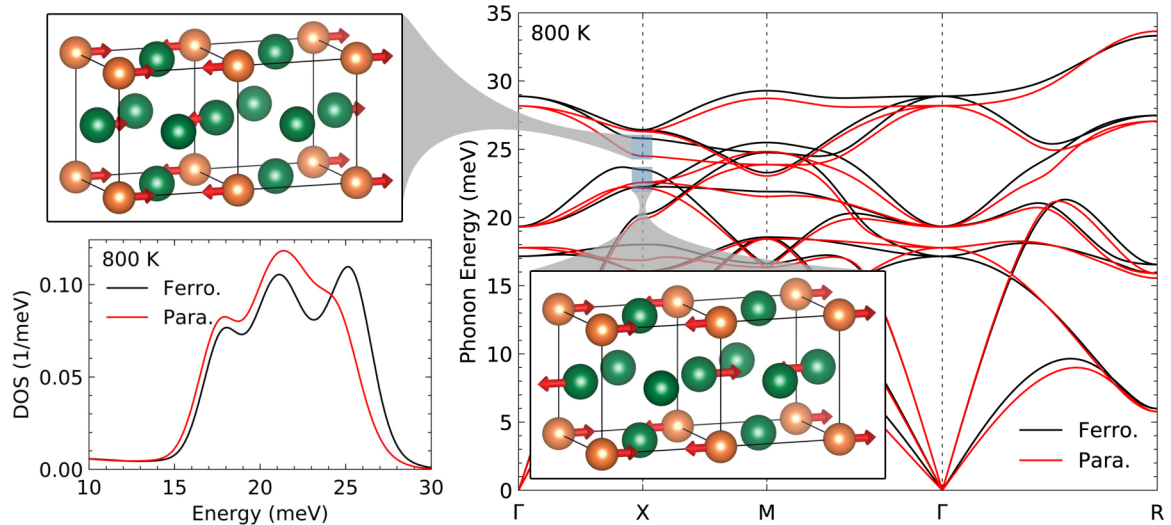


FIG. 9. Calculated phonon dispersions for the ferromagnetic and paramagnetic states at 800 K. The dispersions displayed do not include effects from phonon-phonon interactions. Displacement patterns are shown for two high-energy optical phonon modes that soften with decreasing magnetization. The orange and green spheres represent Fe and Pd atoms, respectively. The Fe partial phonon DOS curves of Pd<sub>3</sub>Fe calculated with the s-TDEP method for the ferromagnetic and paramagnetic states at 800 K are shown in the lower left.

ferromagnetic Pd<sub>3</sub>Fe. These quantities were compared with the quasiharmonic entropy calculated from the QH DFT model.

The  $S_{\text{vib}}^{\text{Fe}}$  of Pd<sub>3</sub>Fe calculated with s-TDEP is lower than what is expected from the QH DFT model by  $0.08k_B/\text{atom}$  at 800 K. The inclusion of PPI increases  $S_{\text{vib}}^{\text{Fe}}$  of Pd<sub>3</sub>Fe by  $0.2k_B/\text{atom}$  at 800 K. The change in  $S_{\text{vib}}^{\text{Fe}}$  from ferromagnetic Pd<sub>3</sub>Fe to Pd<sub>3</sub>Fe with magnetic disorder increases from roughly  $-0.03k_B/\text{atom}$  around the Curie temperature to roughly  $0.1k_B/\text{atom}$  at 800 K. This happens as the deviation from quasiharmonicity sharply increases for ferromagnetic Pd<sub>3</sub>Fe past the Curie temperature.

## IV. DISCUSSION

### A. Magnon-phonon interaction

The increase in Fe partial vibrational entropy with decreasing magnetization at 800 K arises from the softening of Fe vibrational energies with the magnetic transition. A more in-depth analysis of this softening with decreasing magnetization is performed by comparing the 800 K phonon dispersions for both ferromagnetic and paramagnetic Pd<sub>3</sub>Fe, as shown in Fig. 9.

A number of vibrational modes in Pd<sub>3</sub>Fe undergo energy shifts with the randomization of the Fe magnetic moment orientations, particularly the two optical modes at the X symmetry point highlighted in Fig. 9. The softening of these modes contributes to the softening of the high-energy peak in the Fe partial phonon DOS with decreasing magnetization. By testing the sensitivity of the phonon dispersions to changes in each of the quadratic force constants obtained from the fit of Eq. (1) to the Born-Oppenheimer surface, we found that these two modes soften with the weakening of the Fe-Fe second-nearest-neighbor (2NN) longitudinal force constants, which weaken by about 50% from the ferromagnetic state to the paramagnetic state at 800 K. This behavior is consistent

with the atomic displacement patterns for the optical modes, which involve the motions of adjacent (100) planes of Fe atoms in opposite [100] directions. The softening of these modes coincides with a change in the interactions between the closest-neighbor magnetic atoms due to the loss of short-range magnetic order past the Curie temperature.

The average <sup>57</sup>Fe phonon energies from the NRIXS measurements change slowly below the Curie temperature. The s-TDEP calculations for Pd<sub>3</sub>Fe and ferromagnetic Pd<sub>3</sub>Fe show that the thermal evolution of the optical phonons depends on whether the magnetization changes with thermal fluctuations. A thermal optical phonon stiffening in ferromagnetic Pd<sub>3</sub>Fe counteracts the phonon softening from thermal expansion. This behavior is observed in the NRIXS measurements from 298 to 485 K, where Pd<sub>3</sub>Fe still maintains short-range magnetic order. In this case, the short-wavelength optical modes do not soften strongly with temperature, consistent with their behavior in a material with full magnetic order. Beyond the Curie temperature, where there is both long- and short-range magnetic disorder, the change in Fe-Fe interactions cancels this ferromagnetic stiffening of the short-wavelength optical phonons.

### B. Phonon-phonon interaction

The s-TDEP calculations of the phonon DOS of Pd<sub>3</sub>Fe show that anharmonicity has significant effects on the thermodynamics of the material, as indicated by the increase in the Fe partial vibrational entropy by up to  $0.2k_B/\text{atom}$  at 800 K. The anharmonic phonon shifts and broadenings can be studied in more detail with the phonon spectral functions  $S(\mathbf{q}, E)$ , the spectra of lattice excitations that can be interpreted as phonon modes broadened and shifted by phonon-phonon interactions. The spectral function is calculated with  $\omega_{\mathbf{q}s}$ , the phonon dispersion from quadratic force constants, and the real and imaginary components of the phonon self-energy from

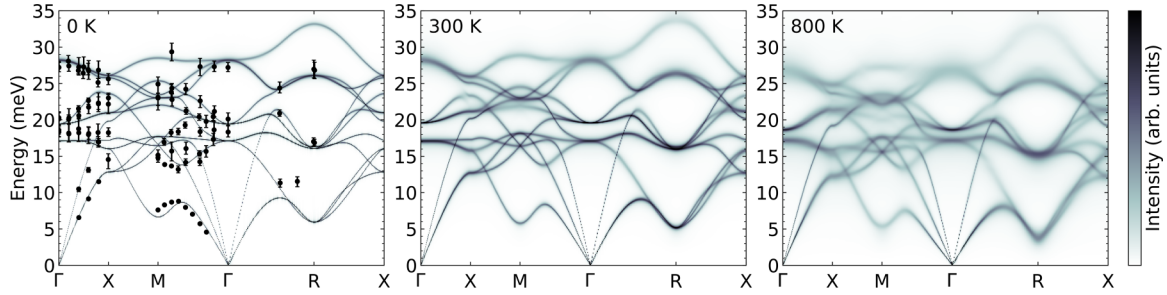


FIG. 10. Pd<sub>3</sub>Fe spectral functions (logarithmic intensity scale) calculated with s-TDEP along the high-symmetry directions at 0, 300, and 800 K. Measurements of the 80 K phonon dispersion by inelastic neutron scattering [60] are shown on top of the 0 K spectral function.

Eqs. (7) and (8):

$$S(\mathbf{q}, E) \propto \sum_s \frac{2\omega_{\mathbf{q}s} \Gamma_{\mathbf{q}s}(\Omega)}{[\Omega^2 - \omega_{\mathbf{q}s}^2 - 2\omega_{\mathbf{q}s} \Delta_{\mathbf{q}s}(\Omega)]^2 + 4\omega_{\mathbf{q}s}^2 \Gamma_{\mathbf{q}s}^2(\Omega)}. \quad (17)$$

The spectral functions shown in Fig. 10 were calculated at multiple temperatures. The 0 K spectral function is in good agreement with the phonon dispersion measured with inelastic neutron scattering at 80 K by Stirling *et al.* [60]. The significant phonon broadening and shifts in the spectral functions at higher temperatures come from many decay channels available to the phonons in the 12 branches.

We examined the line shapes of phonon modes at specific  $\mathbf{q}$  points in the Brillouin zone, including the 800 K line shapes of the phonon modes affected by the magnetic transition at the  $X$  symmetry point, shown in Fig. 11. What was unusual was a double-peak structure of one of these high-energy optical modes. Phonon modes with line shapes that are characterized by a single peak broadened by a Lorentzian are mildly anharmonic, whereas phonon modes that have unusual line shapes are more strongly anharmonic [61,62].

To study the nature of the double peak of the high-energy phonon mode at  $X$ , we analyzed the cubic irreducible force constants responsible for three-phonon interactions. The line shapes at the  $X$  point were calculated when an irreducible force constant was set to zero. It was found that zeroing the cubic force constants for the Fe-Pd first-nearest neighbors (1NNs) along the  $\langle 110 \rangle$  directions partially removes the double-peak

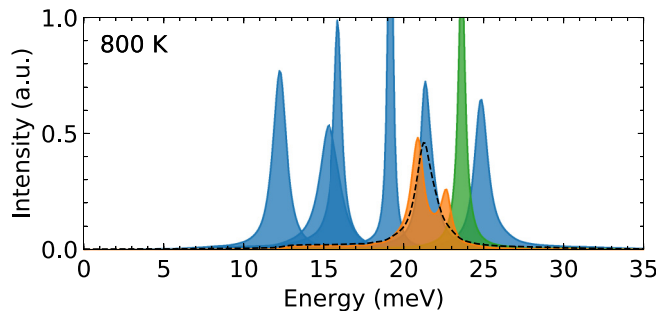


FIG. 11. Pd<sub>3</sub>Fe phonon line shapes at the  $X$  high-symmetry point at 800 K. The orange and green peaks are the optical modes that shift with changing magnetic order. The black dashed peak is the line shape of the optical mode after the Pd-Pd 1NN cubic force constant is set to zero.

structure, but zeroing the cubic force constants for the Pd-Pd 1NN along the  $\langle 110 \rangle$  directions fully transforms the double-peak line shape to a single Lorentzian peak, shown in Fig. 11.

These force constants are related to the movement of Fe and Pd atoms in the  $[100]$  direction against the adjacent stationary  $(200)$  planes of Pd atoms. As shown in the displacement pattern of the vibrational mode in Fig. 9,  $(100)$  planes of Fe atoms and  $(100)$  of Pd atoms alternate in oscillating against the stationary  $(200)$  planes of Pd atoms. The cubic interactions from the oscillation of the  $(100)$  planes of Pd atoms against the  $(200)$  Pd planes more strongly contributes to the unusual phonon line shape. We suggest that the palladium atoms dominate the anharmonic phonon-phonon interactions in  $L1_2$ -ordered Pd<sub>3</sub>Fe. This is consistent with how fcc Pd shows strong PPI at high temperatures [63].

## V. CONCLUSIONS

Nuclear resonant inelastic x-ray scattering was used to measure the <sup>57</sup>Fe partial phonon DOS of  $L1_2$ -ordered Pd<sub>3</sub>Fe from room temperature through the Curie transition. The iron partial vibrational entropy at temperatures far from the Curie transition was observed to be approximately what was predicted by the quasiharmonic approximation owing to a cancellation of effects. A nonharmonic phonon stiffening opposed the expected softening from thermal expansion below the Curie temperature. Similar trends were observed from first-principles calculations that couple the stochastically initialized temperature-dependent effective potential method with magnetic special quasirandom structures of noncollinear magnetic moments.

The s-TDEP calculations showed that phonon-phonon interactions contribute to the softening and broadening of the phonon spectra at elevated temperatures. A high-energy optical mode at the  $X$  symmetry point was calculated to have a double-peak line shape. The first-nearest-neighbor Pd-Pd cubic interactions strongly contribute to this unusual line shape, highlighting the strong contribution of the majority Pd atoms to the phonon anharmonicity in Pd<sub>3</sub>Fe.

The calculations also showed that high-energy optical modes soften with decreasing magnetization, so a ferromagnetic optical phonon stiffening is lost. This softening of optical modes originates from the way the randomization of orientations of the Fe magnetic moments alters the short-range Fe-Fe interactions, softening the Fe-Fe second-nearest-neighbor force constants. The dependence of these optical vibrational modes on the magnetic transition can be understood as the way

magnon-phonon interactions alter lattice vibrations at elevated temperatures.

### ACKNOWLEDGMENTS

This work was supported by the Department of Energy (DOE) through the Capital/DOE Alliance Center, funded by the Department of Energy/National Nuclear Security Administration under Grant No. DE-NA-0002006. The calculations performed herein were made possible by resources of the National Energy Research Scientific Com-

puting Center, a U.S. Department of Energy Office of Science User Facility operated under Contract No. DE-AC02-05CH11231. Portions of this work were performed at HPCAT (Sector 16), Advanced Photon Source (APS), Argonne National Laboratory. HPCAT operations are supported by DOE-NNSA under Award No. DE-NA0001974, with partial instrumentation funding by NSF. The Advanced Photon Source is a U.S. Department of Energy (DOE) Office of Science User Facility operated for the DOE Office of Science by Argonne National Laboratory under Contract No. DE-AC02-06CH11357.

- [1] I. A. Abrikosov, A. V. Ponomareva, P. Steneteg, S. A. Barannikova, and B. Alling, *Curr. Opin. Solid State Mater. Sci.* **20**, 85 (2016).
- [2] P. Steneteg, B. Alling, and I. A. Abrikosov, *Phys. Rev. B* **85**, 144404 (2012).
- [3] N. Shulumba, B. Alling, O. Hellman, E. Mozafari, P. Steneteg, M. Odén, and I. A. Abrikosov, *Phys. Rev. B* **89**, 174108 (2014).
- [4] F. Körmann, A. Dick, B. Grabowski, T. Hickel, and J. Neugebauer, *Phys. Rev. B* **85**, 125104 (2012).
- [5] F. Körmann, B. Grabowski, B. Dutta, T. Hickel, L. Mauger, B. Fultz, and J. Neugebauer, *Phys. Rev. Lett.* **113**, 165503 (2014).
- [6] F. Körmann, A. A. H. Breidi, S. L. Dudarev, N. Dupin, G. Ghosh, T. Hickel, P. Korzhavyi, J. A. Muñoz, and I. Ohnuma, *Phys. Status Solidi B* **251**, 53 (2014).
- [7] Y. Ikeda, F. Körmann, B. Dutta, A. Carreras, A. Seko, J. Neugebauer, and I. Tanaka, *npj Comput. Mater.* **4**, 7 (2018).
- [8] V. P. Antropov, M. I. Katsnelson, M. vanSchilfgaarde, and B. N. Harmon, *Phys. Rev. Lett.* **75**, 729 (1995).
- [9] V. P. Antropov, M. I. Katsnelson, B. N. Harmon, M. vanSchilfgaarde, and D. Kusnezov, *Phys. Rev. B* **54**, 1019 (1996).
- [10] B. Skubic, J. Hellsvik, L. Nordström, and O. Eriksson, *J. Phys.: Condens. Matter* **20**, 315203 (2008).
- [11] L. Mauger, M. S. Lucas, J. A. Muñoz, S. J. Tracy, M. Kresch, Y. Xiao, P. Chow, and B. Fultz, *Phys. Rev. B* **90**, 064303 (2014).
- [12] T. Sohmura, R. Oshima, and F. E. Fujita, *Scr. Metall.* **14**, 855 (1980).
- [13] M. Sugiyama, S. Harada, and R. Oshima, *Scr. Metall.* **19**, 315 (1985).
- [14] Y. Tsunoda and R. Abe, *Phys. Rev. B* **55**, 11507 (1997).
- [15] R. Abe, Y. Tsunoda, M. Nishi, and K. Kakurai, *J. Phys.: Condens. Matter* **10**, L79 (1998).
- [16] B. Dutta, S. Bhandary, S. Ghosh, and B. Sanyal, *Phys. Rev. B* **86**, 024419 (2012).
- [17] Y. O. Kvashnin, S. Khmelevskiy, J. Kudrnovský, A. N. Yaresko, L. Genovese, and P. Bruno, *Phys. Rev. B* **86**, 174429 (2012).
- [18] A. Kussmann and K. Jessen, *J. Phys. Soc. Jpn. Suppl.* **17**, 136 (1962).
- [19] G. Longworth, *Phys. Rev.* **172**, 572 (1968).
- [20] M. L. Winterrose, M. S. Lucas, A. F. Yue, I. Halevy, L. Mauger, J. A. Muñoz, J. Hu, M. Lerche, and B. Fultz, *Phys. Rev. Lett.* **102**, 237202 (2009).
- [21] M. L. Winterrose, L. Mauger, I. Halevy, A. F. Yue, M. S. Lucas, J. A. Muñoz, H. Tan, Y. Xiao, P. Chow, W. Sturhahn, T. S. Toellner, E. E. Alp, and B. Fultz, *Phys. Rev. B* **83**, 134304 (2011).
- [22] See Supplemental Material, which includes Ref. [64], at <http://link.aps.org/supplemental/10.1103/PhysRevB.98.024301> for technical details and results of x-ray diffraction and Mössbauer spectroscopy, raw NRIXS scattering spectra and the multiphonon contributions, Lamb-Mössbauer factors, and a comparison of the scattering data to past measurements.
- [23] A. Chumakov and W. Sturhahn, *Hyperfine Interact.* **123–124**, 781 (1999).
- [24] W. Sturhahn and V. Kohn, *Hyperfine Interact.* **123–124**, 367 (1999).
- [25] W. Sturhahn, *Hyperfine Interact.* **125**, 149 (2000).
- [26] W. Sturhahn and J. M. Jackson, *Geophys. Soc. Am. Special Papers* **421**, 157 (2007).
- [27] O. Hellman, I. A. Abrikosov, and S. I. Simak, *Phys. Rev. B* **84**, 180301 (2011).
- [28] O. Hellman, P. Steneteg, I. A. Abrikosov, and S. I. Simak, *Phys. Rev. B* **87**, 104111 (2013).
- [29] O. Hellman and I. A. Abrikosov, *Phys. Rev. B* **88**, 144301 (2013).
- [30] D. West and S. K. Estreicher, *Phys. Rev. Lett.* **96**, 115504 (2006).
- [31] I. Errea, M. Calandra, and F. Mauri, *Phys. Rev. B* **89**, 064302 (2014).
- [32] N. Shulumba, O. Hellman, and A. J. Minnich, *Phys. Rev. B* **95**, 014302 (2017).
- [33] N. Shulumba, O. Hellman, and A. J. Minnich, *Phys. Rev. Lett.* **119**, 185901 (2017).
- [34] D. S. Kim, O. Hellman, J. Herriman, H. L. Smith, J. Y. Y. Lin, N. Shulumba, J. L. Niedziela, C. W. Li, D. L. Abernathy, and B. Fultz, *Proc. Natl. Acad. Sci. USA* **115**, 1992 (2018).
- [35] P. E. Blochl, *Phys. Rev. B* **50**, 17953 (1994).
- [36] G. Kresse and J. Furthmüller, *Phys. Rev. B* **54**, 11169 (1996).
- [37] G. Kresse and J. Furthmüller, *Comput. Mater. Sci.* **6**, 15 (1996).
- [38] H. Monkhorst and J. Pack, *Phys. Rev. B* **13**, 5188 (1976).
- [39] J. P. Perdew, K. Burke, and M. Ernzerhof, *Phys. Rev. Lett.* **77**, 3865 (1996).
- [40] S. J. Pickart and R. Nathans, *J. Appl. Phys.* **33**, 1336 (1962).
- [41] V. A. Tsurin and A. Z. Men'shikov, *Phys. Met. Metallogr.* **45**, 82 (1978) (in Russian).
- [42] A. Z. Men'shikov and V. A. Tsurin, *Phys. Met. Metallogr.* **47**, 68 (1979) (in Russian).
- [43] A. A. Maradudin and A. E. Fein, *Phys. Rev.* **128**, 2589 (1962).
- [44] R. A. Cowley, *Rev. Prog. Phys.* **31**, 123 (1968).
- [45] A. Zunger, S.-H. Wei, L. G. Ferreira, and J. E. Bernard, *Phys. Rev. Lett.* **65**, 353 (1990).
- [46] B. Alling, T. Marten, and I. A. Abrikosov, *Phys. Rev. B* **82**, 184430 (2010).

- [47] J. Hubbard, *Phys. Rev. B* **19**, 2626 (1979).
- [48] J. Hubbard, *Phys. Rev. B* **20**, 4584 (1979).
- [49] J. Hubbard, *Phys. Rev. B* **23**, 5974 (1981).
- [50] H. Hasegawa, *J. Phys. Soc. Jpn.* **46**, 1504 (1979).
- [51] H. Hasegawa, *J. Phys. Soc. Jpn.* **49**, 178 (1980).
- [52] B. L. Gyorffy, A. J. Pindor, J. Staunton, G. M. Stocks, and H. Winter, *J. Phys. F* **15**, 1337 (1985).
- [53] G. Inden, in *Proceedings Project Meeting, CALPHAD V* (Max Planck Institut. für Eisenforschung, Düsseldorf, 1976), pp. 1–13.
- [54] M. D. Kuz'min, *Phys. Rev. Lett.* **94**, 107204 (2005).
- [55] W. Sturhahn and E. Gerdau, *Phys. Rev. B* **49**, 9285 (1994).
- [56] L. Mauger, J. E. Herriman, O. Hellman, S. J. Tracy, M. S. Lucas, J. A. Muñoz, Y. Xiao, J. Li, and B. Fultz, *Phys. Rev. B* **95**, 024308 (2017).
- [57] D. C. Wallace, *Thermodynamics of Crystals* (Dover, Mineola, NY, 1998).
- [58] D. C. Wallace, *Statistical Physics of Crystals and Liquids: A Guide to Highly Accurate Equations of State* (World Scientific, Singapore, 2002).
- [59] J. Jääskeläinen and E. Suoninen, *Phys. Status Solidi A* **63**, 241 (1981).
- [60] W. G. Stirling, R. A. Cowley, and M. W. Stringfellow, *J. Phys. F* **2**, 421 (1972).
- [61] O. Delaire, J. Ma, K. Marty, A. F. May, M. A. McGuire, M.-H. Du, D. J. Singh, A. Podlesnyak, G. Ehlers, M. D. Lumsden, and B. C. Sales, *Nat. Mater.* **10**, 614 (2011).
- [62] C. W. Li, O. Hellman, J. Ma, A. F. May, H. B. Cao, X. Chen, A. D. Christianson, G. Ehlers, D. J. Singh, B. C. Sales, and O. Delaire, *Phys. Rev. Lett.* **112**, 175501 (2014).
- [63] Y. Shen, C. W. Li, X. Tang, H. L. Smith, and B. Fultz, *Phys. Rev. B* **93**, 214303 (2016).
- [64] A. P. Hammersley, S. O. Svensson, M. Hanfland, A. N. Fitch, and D. Häusermann, *High Pressure Res.* **14**, 235 (1996).